Dynamic stability in spinor Bose gases in moiré lattices with square and hexagonal symmetries

C. Madroñero and R. Paredes[*]

Instituto de Física, Universidad Nacional Autónoma de México, Apartado Postal 20-364, México D.F. 01000, Mexico

A broad range of phenomena in correlated electrons traveling in moiré lattices has emerged in both scenarios, experiments and theory. In this paper we report the observation of a dynamic stability that arises in an analogous system to that of electrons, a weakly interacting spinor Bose gas of ultracold ^{23}Na atoms lying in a single layer having a moiré pattern with square and hexagonal symmetries. Our paper is based on the dynamical description of two magnetic domains represented by two hyperfine spin components of a Bose condensate initially localized in the left and right halves of a moiré lattice defined by a specific angle θ plus a harmonic confinement. To demonstrate the persistence of such an initial condition under the competence of the moiré pattern and harmonic confinements we studied both single noninteracting and double-domain interacting cases. We solve the time dependent Gross-Pitaevskii equations, and track the time evolution of several observables on each half as a function of the twisting angle. In the case of square moiré lattices we found a dynamic stability for angles larger than a special one θ_s, except for the Pythagorean angles. The value of such an angle depends on the existence of a harmonic trap when interactions are absent, while this dependence is negligible for the interacting case. Hexagonal moiré lattices exhibit the dynamic stability starting from a certain angle that also depends on the harmonic confinement for the noninteracting case.

I. INTRODUCTION

The investigation here addressed is connected with the phenomenology and physical properties arising in two-dimensional (2D) structures, in particular, with the properties persisting in patterns formed when two periodic lattices lie on top of each other with a relative twist between them. In recent years exotic transport and magnetic properties have been measured in assemblies of monolayers of transition-metal dichalcogenides [1–4]. It is believed that as a result of the incommensurate lattice structure arising from the interlayer twist, and/or lattice constant mismatch, anomalous interlayer couplings are originated, and consequently, profound effects on the transport and optical properties in the bilayer arrays arise. This novel class of 2D materials exhibits ultrafast interlayer charge transfer that facilitates the photocurrent generation and the formation of interlayer excitons. Even more, twisted bilayer graphene has been demonstrated to exhibit superconductivity for the so-called magic angles of rotation [5], correlated insulating behavior [6], and magnetization textures in 2D magnets [7]. Even more, it has been proven that in certain mixtures there exist other rotation angles for which unexpected properties arise, as the emergence of flat bands [8].

The theoretical study of properties rising in twisted bilayers has been addressed from several routes. While the emergence of superconductivity for the magic angles was explained in terms of a continuum model that predicts flats bands [9], the emergence of ferromagnetism was predicted in twisted bilayer graphene using first-principles density-functional theory calculations [10,11]. An effective model has suggested

the existence of a ferromagnetic Mott insulator for maximally localized Wannier wave functions in twisted graphene bilayers [12]. The phase diagram at mean-field level for a moiré-Hubbard model has revealed a variety of phases including Wigner crystals with charge-density wave forms and Chern insulators [13]. Perhaps the most common feature found in those theoretical investigations is the existence of a particular angle of rotation among graphene layers for which phases and particular properties are displayed.

The interest of the present paper is to establish how the appearance of a dynamic stability can be controlled by the twisting angle between two primitive lattices with either square or honeycomb 2D structure. To accomplish this purpose we consider an analogous system to electrons traveling through ion cores of a 2D solid having a moiré pattern, a weakly interacting bicomponent Bose gas in its ground state confined in a 2D moiré pattern of light. In particular, we track the dynamics of a double magnetic domain that evolves under the influence of either square or hexagonal moiré patterns plus a harmonic confinement. Although such a harmonic constraint does not have its analogy in solid state, it is generally present in experiments with ultracold Bose gases. Three years ago a theoretical proposal considered cold bosons confined in a bilayer in which it is possible to control the inter- and intralayer coupling [14]. Such an array, in which a spinor Bose-Einstein condensate is loaded into spin-dependent optical lattices that form the moiré structure, is the ideal scenario to investigate the physics behind the superconductivity in twisted-bilayer graphene [15]. Other techniques through which optical moiré patterns can be created are by means of laser interference lithography [16] or digital micromirror devices [17,18]. Regarding the role of the electron-electron interactions, they have also their counterpart in bosonic samples in their

---

*rosario@fisica.unam.mx

degenerate state. Indeed, interactions in ultracold atoms can be varied by adjusting either the effective interaction coupling or the condensate density. In our paper we shall consider the largest size of the lattices for which our numerical experiments can be performed, lattices with $\approx 90 \times 90$ sites. The evolution for sufficiently long times resulting from the coupled time-dependent Gross-Pitaevskii (GP) equations revealed a dynamic stability of the initial state. Such stability disappears in two different situations: for moiré lattices associated with angles belonging to an interval that diminishes as the effective interatomic interaction is increased, or for angles coming from Pythagorean triples in the case of square moiré lattices. In the case of hexagonal moiré lattices, there are certain angles satisfying a Diophantine equation that promote a slowdown in the dynamics.

The paper is structured as follows. First in Sec. II we present the coupled equations that characterize the dynamics of two hyperfine spin components. Then, in Sec. II we explain how to generate the initial state composed of two magnetic domains lying in definite moiré patterns. Afterwards, in Sec. III we discuss the dynamics developed by the ferromagnetic state as a function of the angle that defines a given moiré pattern for both noninteracting (Sec. III A) and weakly interacting (Sec. III B) cases. Finally, we summarize our findings in Sec. IV, and provide an outlook of future directions of our paper.

II. TWO-COMPONENT BOSE GAS CONFINED IN MOIRÉ LATTICES

In this section we establish the model to describe the dynamics of two magnetic domains evolving under the influence of weak interactions among its constituents, and lying in moiré lattices plus a harmonic confinement. The single layer moiré structures that we shall consider result from superimposing a pair of 2D rotated square or hexagonal lattices. Our particular interest is to establish the persistence of a given initial state formed by two hyperfine spin components lying on a moiré structure. The initial state that we consider will be set, as described in Sec. II, with two halves in which a couple of different spin components of sodium atoms are placed. As described in the Introduction, the system under study belongs to the ultracold quantum matter context, a weakly interacting $F = 1$ spinor Bose condensate on ^{23}Na atoms confined in a 2D optical lattice having a moiré like structure. Particularly, we concentrate on the dynamics of two hyperfine spin components, $|\uparrow\rangle = |F = 1, m_F = 1\rangle$ and $|\downarrow\rangle = |F = 1, m_F = -1\rangle$, lying in the 2D moiré lattices, represented by $V_{\text{ext}}(\vec{r})$. The importance of selecting a particular atomic species relies in the necessity of having a system whose nature is a polar one [19]. Within the mean-field formalism the wave functions $\Psi_\uparrow$ and $\Psi_\downarrow$ of the two species $|\uparrow\rangle$ and $|\downarrow\rangle$, respectively, obey the following effective coupled GP equations:

$$i\hbar \frac{\partial \Psi_\uparrow(\vec{r}, t)}{\partial t} = [H_0(\vec{r}) + g_{\uparrow\uparrow}|\Psi_\uparrow|^2 + g_{\downarrow\uparrow}|\Psi_\downarrow|^2]\Psi_\uparrow(\vec{r}, t),$$

$$i\hbar \frac{\partial \Psi_\downarrow(\vec{r}, t)}{\partial t} = [H_0(\vec{r}) + g_{\downarrow\downarrow}|\Psi_\downarrow|^2 + g_{\uparrow\downarrow}|\Psi_\uparrow|^2]\Psi_\downarrow(\vec{r}, t), \quad (1)$$

where $H_0(\vec{r}) = -\frac{\hbar^2}{2m}\nabla_\perp^2 + V_{\text{ext}}(\vec{r})$ with $\nabla_\perp^2 = \frac{\partial^2}{\partial x^2} + \frac{\partial^2}{\partial y^2}$ is the Laplacian operator in 2D, m is the equal mass of the two spin components, and $\vec{r} = x\hat{i} + y\hat{j}$. The external potential in 2D has the following form:

$$V_{\text{ext}}(x, y) = \begin{cases} V_{\text{HO}}(x, y) + \frac{1}{2}[V_{\text{sq}}(x, y) + V_{\text{sq}}(x', y')] \\ V_{\text{HO}}(x, y) + \frac{1}{2}[V_{\text{hex}}(x, y) + V_{\text{hex}}(x', y')] \end{cases} \quad (2)$$

where $V_{\text{HO}}(x, y) = \frac{1}{2}m(\omega_x^2 x^2 + \omega_y^2 y^2)$ is a harmonic oscillator, that is usually present when an ultracold gas is produced in a laboratory. The values of the frequencies that we shall consider for our analysis are $\omega_x = \omega_y = \omega_r$, where $\omega_r/\omega_0 = 0, 0.4, 0.7$, and 1, with $\omega_0 = 2\pi \times 50$ rad/s; this value of the frequency is a typical one in experiments with ultracold atoms [20,21]. The variables x' and y' belong to a system rotated an angle θ as follows:

$$\begin{pmatrix} x' \\ y' \end{pmatrix} = \begin{pmatrix} \cos\theta & -\sin\theta \\ \sin\theta & \cos\theta \end{pmatrix} \begin{pmatrix} x \\ y \end{pmatrix}. \quad (3)$$

The second contribution of Eq. (2) is the term from which emerge the square and hexagonal moiré lattices, each lattice being given by

$$V_{\text{sq}}(x, y) = V_0[\cos^2(kx) + \cos^2(ky)],$$

$$V_{\text{hex}}(x, y) = V_0\left[\cos\left(\frac{4ky}{3}\right) + \cos\left(\frac{2kx}{\sqrt{3}} - \frac{2ky}{3}\right) \right.$$

$$\left. + \cos\left(\frac{2kx}{\sqrt{3}} + \frac{2ky}{3}\right) \right]. \quad (4)$$

Regarding the values of the effective interaction couplings $g_{\sigma\sigma'}$ with $\sigma, \sigma' = \{\uparrow, \downarrow\}$, they are written in terms of the s-wave scattering lengths a_i, with $i = 0$ and 2 being the labels of collision channels 0 and 2, respectively. In $g_{\uparrow\uparrow} = g_{\downarrow\downarrow} = 4\pi N\hbar^2 a_2/m$ and $g_{\downarrow\uparrow} = 4\pi N\hbar^2/m(\frac{2a_0+a_2}{3})$, N is the number of particles of each component in the condensate, with $N = N_\uparrow = N_\downarrow$. It is worth pointing out that the nature of the ground state of the hyperfine components of ^{23}Na atoms is polar as a consequence of the condition $a_0 < a_2$ [22,23]. This inequality guarantees the possibility that the hyperfine components can be mixed as they evolve in time given an initial state. In this paper we shall analyze the role of the effective interaction $g_{\sigma,\sigma'}$ by varying N, ensuring that the hyperfine components are far from the Mott insulating phase. It is important to stress here that since originally the GP equation describes the ground state of the condensate in three dimensions, these interaction coefficients must be substituted by effective interaction couplings that take into account that the atom collision processes occur in 2D [24–30]. The effective scattering length in the plane x-y becomes $a_i \rightarrow a_i/\sqrt{2\pi}l_z$, with $l_z = \sqrt{\hbar/m\omega_z}$, ω_z being a typical frequency of condensates confined in 2D [20,21]. The potential depth is scaled in units of the recoil energy $E_R = \frac{\hbar^2 k^2}{2m}$, where $k = \pi/a$ and a are the lattice constants of the primitive square and hexagonal lattices. As previously shown in the literature, the mean-field approximation describes well the dynamics of initial magnetic domains, that evolve in time under given conditions [31–35].
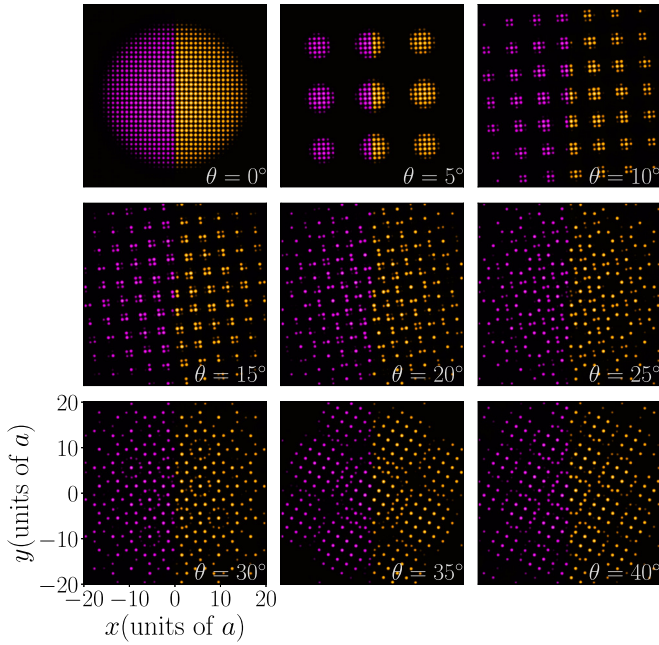
FIG. 1. Density profiles prepared from the superposition of two square lattices rotated a twisting angle θ. Left (purple) and right (yellow) sides correspond to the superfluid density associated to the spin components $\downarrow$ and $\uparrow$. Frequency of the harmonic trap is $\omega_r = 0.4\omega_0$.

Preparation of the initial state

The initial state associated to a given angle θ for which a double ferromagnetic state lies in a moiré lattice, either square or hexagonal, is set as we describe in the next lines. First we determine the stationary state for the coupled equations (1) for optical lattices defined by the potential $V_{ext}(x, y)$, having a constant depth $V_0/E_R = 2$. For this purpose free-energy minimization is performed by means of imaginary time evolution $\tau \to it$ [36–38]. After this procedure, we manually remove the particles having spin component $\sigma = \uparrow$ from the left half layer, while we remove particles with $\sigma = \downarrow$ from the right half layer. In Figs. 1 and 2 we plot some of the density profiles prepared as the initial state for the square and hexagonal moiré structures, respectively. The frequency of the harmonic trap in these figures is $\omega_r = 0.4\omega_0$. At the bottom of each subfigure the twisting angle is indicated. Purple and yellow colors identify the density profiles of the $\downarrow$ and $\uparrow$ components. Notice that equal ground-state densities of different hyperfine states remain at each half in the 2D moiré lattices. The removal of particles proposed to set these initial states mimics experimental procedures in which a digital mirror device is used to optically remove the particles at specific positions [17,18]. Certainly, another route to achieve ferromagnetic domains is by means of a magnetic field [39]. These patterns manually created, the two ferromagnetic domains for a given value of the twisting angle θ, are our starting point to study its time evolution under the influence of the moiré confinement. We should note here that the initial state prepared for each angle θ is nonstationary, and consequently it evolves under their own dynamics. We must point out that this kind of state from which a system evolves under its own dynamics
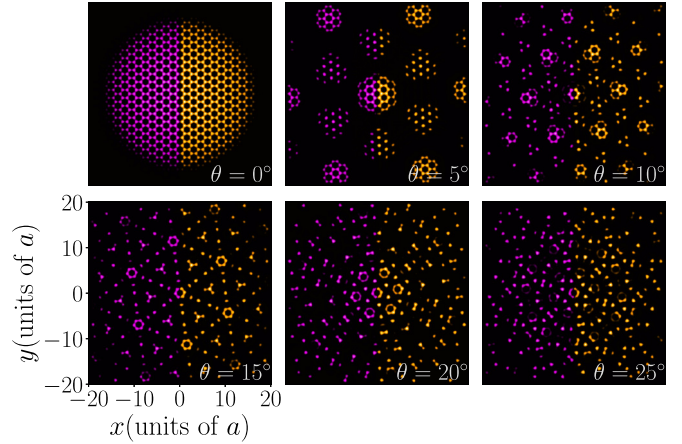

FIG. 2. Density profiles prepared from the superposition of two rotated hexagonal lattices rotated a twisting angle θ. Left (purple) and right (yellow) sides correspond to the superfluid density associated to the spin components $\downarrow$ and $\uparrow$. Frequency of the harmonic trap is $\omega_r = 0.4\omega_0$.

is the so-called quantum quench created in the laboratory. Our particular interest is to investigate how the local magnetization of the ferromagnetic domains evolves in a weakly interacting 2D Bose mixture in the absence of other external fields, except the one produced from the superposition of the lattices forming the moiré patterns associated to either square or hexagonal moiré patterns. It is important to mention that the effective coupling interaction coefficients must be rescaled for $t > 0$ since half of the population is removed to have the magnetic domains, that is, $2N \to N$. Due to the symmetry of the lattices, the twisting angles that shall be considered for the analysis of the evolution in time are $\theta \in (0°, 30°]$ and $(0°, 45°]$ for the hexagonal and square lattices, respectively. Angles larger than those produce the same results because of the mirror symmetry.

III. DYNAMICS OF A DOUBLE MAGNETIC DOMAIN IN MOIRÉ LATTICES

The physical observable that accounts for the magnetic character of the system here analyzed is the spin texture. This quantity is defined as

$$\mathbf{T}(x, y, t) = \Psi^{\dagger}(x, y, t)\hat{\mathbf{F}}\Psi(x, y, t), \quad (5)$$

where the operator $\hat{\mathbf{F}}$ is written in terms of the Pauli matrices $\hat{\mathbf{F}} = (\hat{\sigma}_x, \hat{\sigma}_y, \hat{\sigma}_z)$, and $\Psi(x, y, t) = (\Psi_{\uparrow}(x, y, t), \Psi_{\downarrow}(x, y, t))$. Thus the spin texture, which is a real quantity, is given by

$$\mathbf{T}(x, y, t) = [\Psi_{\uparrow}^*\Psi_{\downarrow} + \Psi_{\uparrow}\Psi_{-\downarrow}^*]\hat{x} + i[\Psi_{\uparrow}^*\Psi_{\downarrow} - \Psi_{\uparrow}\Psi_{\downarrow}^*]\hat{y}$$
$$+ [|\Psi_{\uparrow}|^2 - |\Psi_{\downarrow}|^2]\hat{z}. \quad (6)$$

The component along axis $\hat{z}$ is the local magnetization at time t. This is precisely the observable that we shall track to determine in a quantitative way either the persistence or the absence of the initial state as a function of time, for a given value of the twisting angle θ. In addition, we must emphasize that this observable is the natural quantity that can be accessed in typical experiments with ultracold atoms [40], or

within the context of condensed matter. The observables to be studied are the magnetizations m_L and m_R, in the left and right sides of the lattice, as a function of time for different values of θ, and as stated above, for given values of the coupling interaction. These quantities are defined in terms of the local magnetization $m(x, y; t) = \rho_\uparrow(x, y; t) - \rho_\downarrow(x, y; t)$, where $\rho_\uparrow(x, y; t)$ and $\rho_\downarrow(x, y; t)$ are the densities associated with the components $\uparrow$ and $\downarrow$, respectively. Thus, magnetizations in left and right sides are

$$m_L = \iint_{\Omega_L} dx\, dy\, m(x, y; t),$$

$$m_R = \iint_{\Omega_R} dx\, dy\, m(x, y; t), \tag{7}$$

where Ω_L and Ω_R are the left and right halves of the system, respectively. Because of the particular election of the initial state we have that $m_L(t = 0) = -0.5$ and $m_R(t = 0) = 0.5$.

The evolution in time of the initial states will be followed in dimensionless time $\tau = E_R t / \hbar$. It is important to mention here that all of our numerical calculations were performed ensuring that changing $\tau \to -\tau$, at any temporal step along the time dynamics, allows us to recover the initial state. The time during which the magnetization in left and right sides will be tracked coincides with that at which the magnetization in both sides becomes null for a twisting angle $\theta = 0°$. In other words, the magnetization associated with $\theta = 0°$ when no moiré patterns exist provides a reference in terms of which one can evaluate the influence of changing the angle θ, either diminishing or preserving the magnetization. As we describe below, the presence of the harmonic confinement also plays a role in the evolution of the given initial state.

A. Noninteracting case

For comparison purposes with the weakly interacting scenario, we first analyze the time evolution of the noninteracting bosonic mixture given the initial ferromagnetic state described in the previous section. That is, we solve the Schrödinger equation that corresponds to set $g_{\sigma\sigma'} = 0$ for σ, $\sigma' = \{\uparrow, \downarrow\}$. As stated in the above paragraphs, the magnetization was followed for a time interval in which it becomes null. In Fig. 3 we plot the magnetization on the right side for square (top panel) and hexagonal (bottom panel) structures. Different lines correspond to different values of ω_r. The behavior shown in these figures is the starting point to analyze the dynamics of moiré lattices, namely, when the rotation angle is nonzero. It is worth noting that magnetization on the left and right sides satisfies $m_R(\tau) = -m_L(\tau)$. As the angle θ varies, one can appreciate how magnetization on the right side suffers a distortion with respect to $\theta = 0°$ (see Fig. 3). To illustrate these modifications, in the main panels of Figs. 4 and 5 we plot the magnetization on the right side for $\theta = 5°$ and $30°$, and $\theta = 10°$ and $25°$ for square and hexagonal lattices, respectively. In the insets of the bottom panels in these figures we plot the magnetization as a function of time for the whole range of angles considered in our analysis. As can be seen from the main panels in Figs. 4 and 5, m_R shows oscillations of large amplitude for $\theta = 5°$ and $10°$, while there is an almost imperceptible variation for $\theta = 30°$ and $25°$ for square
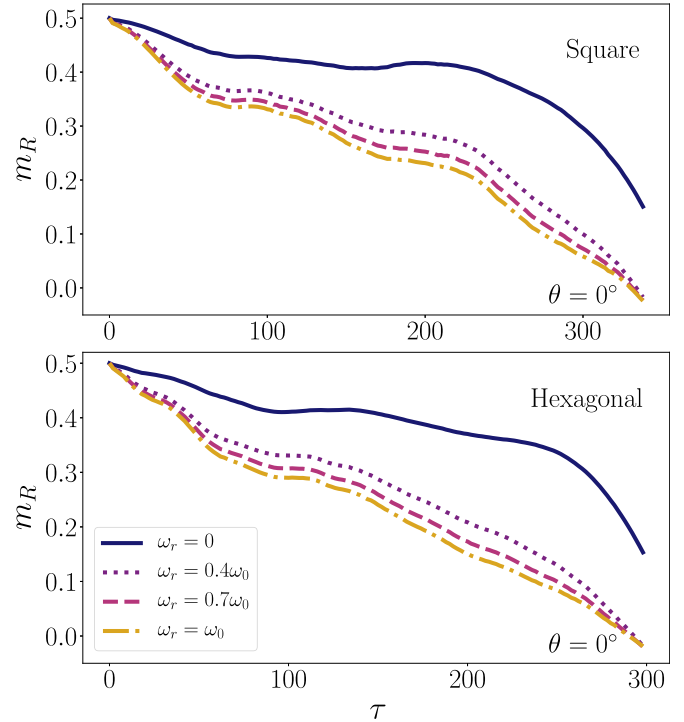

FIG. 3. Magnetization as a function of time in the right side in square (top panel) and hexagonal (bottom panel) lattices. Different curves in both panels are associated with the size of the harmonic confinement as indicated in the bottom panel. (noninteracting case).

and hexagonal lattices, respectively. It is important to notice that the oscillation period for $\theta = 5°$ and $10°$ for square and hexagonal lattices, respectively, is independent of the value of the frequency ω_r. This behavior must be related with the type of moiré lattice that emerges as the rotation angle θ varies. In Appendix A we analyze the stationary states that arise in two square and two hexagonal rotated lattices. From the insets of bottom panels in Figs. 4 and 5 that condense the entire information of $m_R(\tau)$ in terms of the rotation angle, interesting facts can be noticed. On one side we have the existence of a sharp transition at a special value of the angle, that here and henceforth we shall call θ_s.

To appreciate the transition, as well as have a proper identification of θ_s, we make an amplification near the values of θ where the magnetization develops the abrupt change. In Figs. 6 and 7 we show the behavior of m_R in these regions. As one can appreciate, a crossover replaces the abrupt transition. In other words, considering shorter intervals of the angles where the change occurs, $\Delta\theta$, leads us to recognize a region of rotation angles, namely, certain moiré crystals, in which a dynamic stability disappears. One can also see that the angle at which the abrupt transition occurs depends on whether the harmonic frequency is zero or nonzero only. As can be seen from Fig. 6, we have that if $\omega_r = 0$ then $\theta_s \approx 3.5°$, while if $\omega_r \neq 0$ then $\theta_e \approx 11.98°$ for lattices with square symmetry. Regarding the lattices with hexagonal symmetry, as illustrated in Fig. 7, we found that if $\omega_r = 0$ then $\theta_s \approx 4.77°$, while if $\omega_r \neq 0$ then $\theta_s \approx 13.88°$.

In the case of the square moiré patterns, for angles larger than those belonging to the yellow region, one can recognize
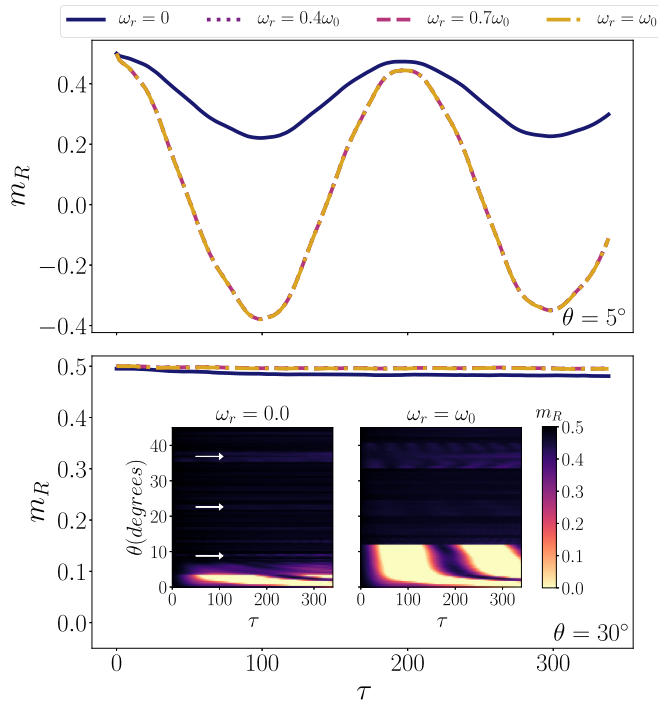
FIG. 4. Magnetization as a function of time in the right side of a moiré pattern created from the superposition of two square lattices rotated an angle θ. Panels on top and bottom correspond to $\theta = 5°$ and $30°$, respectively. Different lines in both panels are associated with the size of the harmonic confinement as indicated in the top panel. The insets at the bottom figure are the value of the magnetization as a function of time for the whole range of angles considered in our analysis.
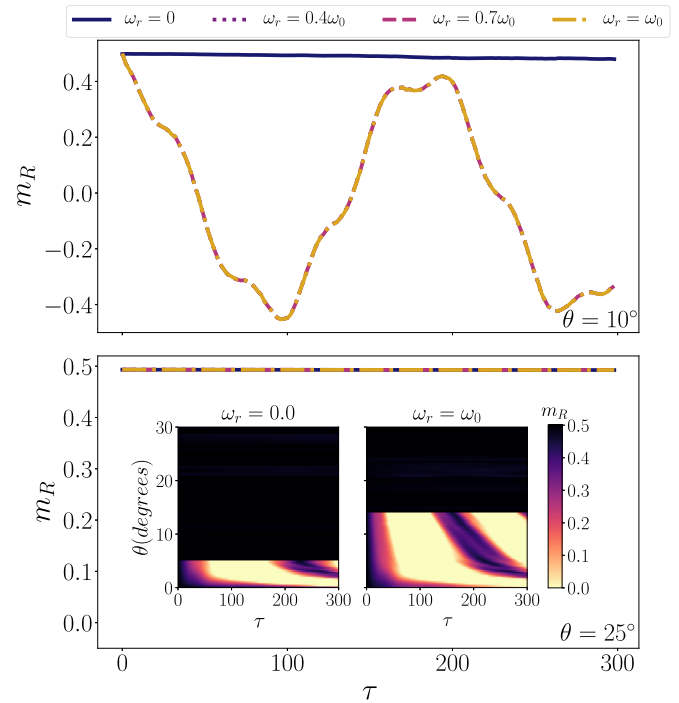
FIG. 5. Magnetization as a function of time in the right side of a moiré pattern created from the superposition of two hexagonal lattices rotated an angle θ. Panels on top and bottom correspond to $\theta = 10°$ and $25°$, respectively. Different lines in both panels are associated with the size of the harmonic confinement as indicated in the top panel. The insets in the bottom figure are the value of the magnetization in the right side as a function of time for the whole range of angles considered in our analysis.

particular values of θ for which the magnetization decreases (see white arrows in dark zones of Fig. 4). This behavior of m_R for special angles is associated with particular values of integer numbers m and n such that $\tan \theta = n/m$. These numbers satisfy the Diophantine equation $m^2 + n^2 = l^2$, with l being also an integer number [41]. The angles satisfying the previous condition are called Pythagorean, while the sets (m, n, l) are known as Pythagorean triples. Besides the regions indicated with white arrows, there are some other angles for which the magnetization shows the mentioned decay, but they are not visible with respect to the color scale in Fig. 4. In fact, there are 14 additional Pythagorean angles for the square lattice. In other sublattices where the primitive cell is not a square, as the hexagonal one, the Diophantine equation satisfied by the triples is $m^2 + n^2 + nm = l^2$, and $\tan \theta = n\sqrt{3}/(2m + n)$, (m, n, l) being integer numbers. Surprisingly, in photonic moiré lattices [41] light propagation shows signatures similar to those found in matter, namely, a localized-extended transition occurs. As we shall see in the next section, when interactions are considered, Diophantine angles show a reminiscent localized-extended behavior exhibited in the case of light.

The above findings, that is, the dynamics in the absence of interactions, suggest that the stability is not related with the spin imbalance but with the presence of the moiré lattice. To better appreciate the emergence of the transition at special angles, we introduce an observable that quantifies the

probability that a wave function initially localized on the right side remains there for a large enough time. For this analysis we select the $\uparrow$ component. We evaluate the following quantity:

$$\langle I_{\Omega_R} \rangle = \frac{1}{\tau_0} \int_0^{\tau_0} dt \int_{\Omega_R} dx \, dy \, \rho_\uparrow(x, y; t), \qquad (8)$$
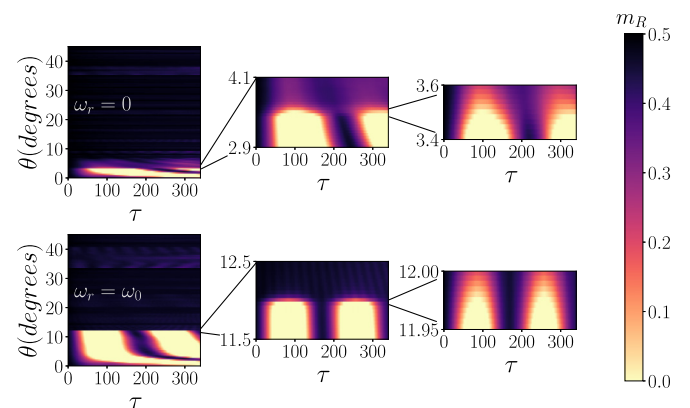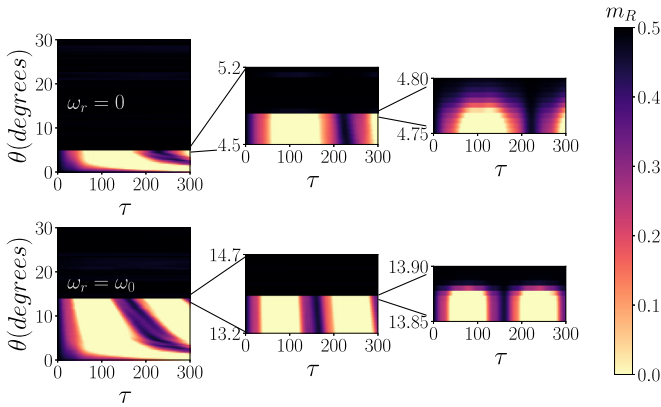

FIG. 6. Magnetization as a function of time plotted in a density color scheme. The angle in the vertical axis corresponds to the rotation angle that defines moiré patterns created from the superposition of two square lattices rotated an angle θ. (noninteracting case).

FIG. 7. Magnetization as a function of time plotted in a density color scheme. The angle in the vertical axis corresponds to the rotation angle that defines moiré patterns created from the superposition of two hexagonal lattices rotated an angle θ (noninteracting case).

where the time τ_0 corresponds to twice the time interval in which the magnetization on the right side becomes null in the absence of moiré confinement, that is, when the rotation angle is $\theta = 0$ (see Fig. 3). In Figs. 8 and 9 we illustrate the behavior of $\langle I_{\Omega_R} \rangle$ as a function of the rotation angle θ for square and hexagonal lattices, respectively. The main panels in these figures show the behavior of $\langle I_{\Omega_R} \rangle$ for the whole range of angles analyzed in both geometries. The insets in these
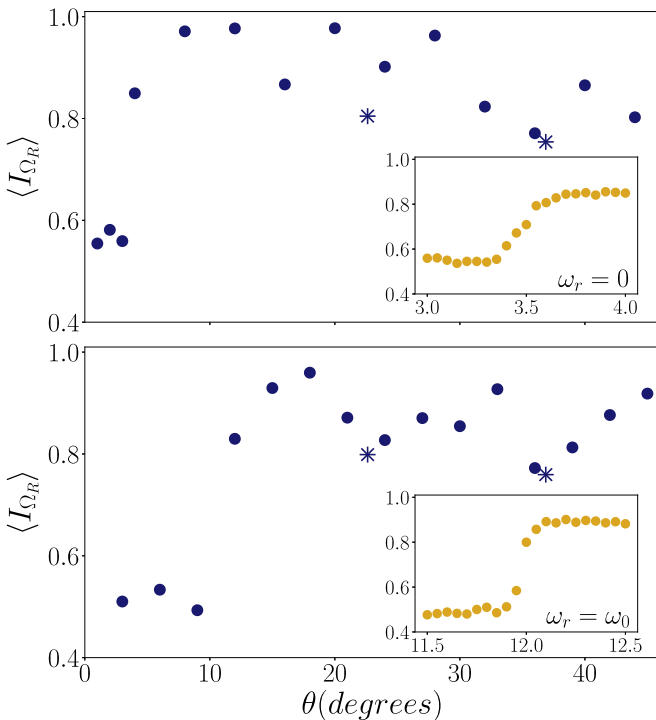

FIG. 8. Time average of density in the right side, $\langle I_{\Omega_R} \rangle$, as a function of the rotation angle that generates the square moiré lattice. Upper and lower panels correspond to two different values of the harmonic frequency $\omega_r = 0$ and ω_0. The insets show a restricted region of the angles where the transition from extended to localized transition is better appreciated.
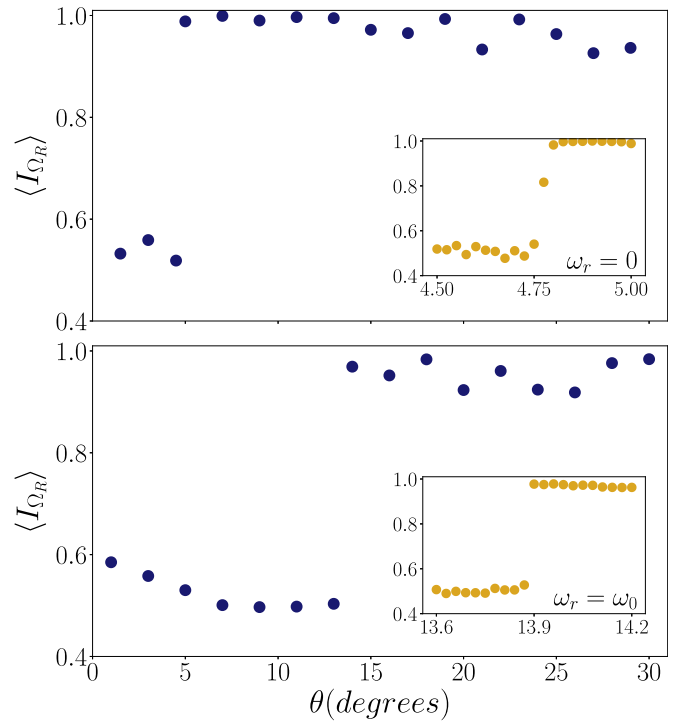

FIG. 9. Time average of density in the right side, $\langle I_{\Omega_R} \rangle$, as a function of the rotation angle that generates the hexagonal moiré lattice. Upper and lower panels correspond to two different values of the harmonic frequency $\omega_r = 0$ and ω_0. The insets show a restricted region of the angles where the transition from extended to localized transition is better appreciated.

figures correspond to a restricted region of the angles where the transition is better appreciated (see yellow dots). Upper and lower panels in each figure correspond to two different values of the harmonic frequency $\omega_r = 0$ and ω_0.

The points labeled with an asterisk in Fig. 8 correspond to values of θ associated with diophantine triads. If the wave function remains at the half where it was placed, Ω_R, then one recognizes a localized state and the value of $\langle I_{\Omega_R} \rangle$ approaches 1. In contrast, if the wave function distributes across the whole space, then the value of the quantity will be near 0.5. We should point out that in the case of Pythagorean angles $\langle I_{\Omega_R} \rangle$ is less than 1. As stated above Pythagorean angles are labeled with asterisks.

We must stress that the analysis for the noninteracting case reveals the crucial role that the twist angle has on the identification of the sharp transition. Here we must point out the analogous behavior of this finding and that exhibited in graphene van der Waals heterostructures, as well as light localization in photonic moiré lattices [6,41].

B. Weakly interacting case

In the next paragraphs we shall characterize the evolution of the initial ferromagnetic state through the study of the magnetization as a function of both the rotation angle that defines the moiré pattern and the amplitude of the effective mean-field interaction $g_{\sigma\sigma'}$. In Fig. 10 we plot the magnetization on the right side for $\theta = 0°$ for $N = 300$. Top and bottom panels
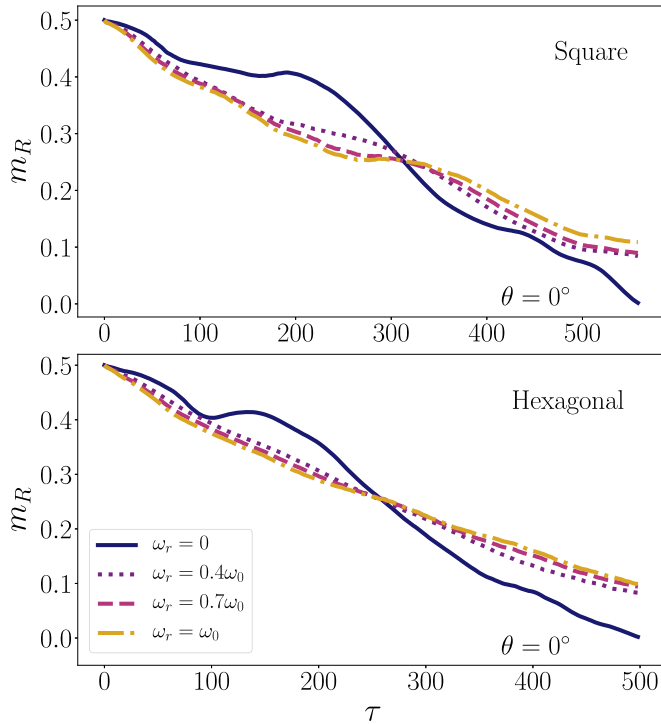
FIG. 10. Magnetization as a function of time in the right side in square (top panel) and hexagonal (bottom panel) lattices. Different curves in both panels are associated with the size of the harmonic confinement as indicated in the bottom panel. The effective interaction coupling $g_{\downarrow\downarrow} = 4\pi N\hbar^2 a_2/m$ and $g_{\downarrow\uparrow} = 4\pi N\hbar^2/m(\frac{2a_0+a_2}{3})$ with $N = 300$.

correspond to square and hexagonal structures, respectively. One can appreciate from these figures the influence of the effective interaction in the demagnetization process in the primitive square and hexagonal lattices. While for $g_{\sigma\sigma'} = 0$ the initial domains are destroyed around $\tau \approx 300$, in the weakly interacting case the ferromagnetic state in left and right sides is retained for longer times, $\tau \approx 500$.

In analogy with the noninteracting case, the scenario completely changes when the two superimposed lattices are rotated with respect to one other. Taking as a reference the behavior of the magnetization for $\theta = 0°$, we proceed with the analysis of the magnetization dynamics as a function of θ for the square and hexagonal moiré patterns, considering also the influence of the effective interaction strength $g_{\sigma\sigma'}$. The main conclusion is the identification of a set of twisting angles for which the initial state is preserved. For the square lattice this set is $[\theta_s, 45°]$, excluding the Pythagorean angles. For the hexagonal lattices the interval of angles for which the dynamic stability exists is $[\theta_s, 30°]$. We should point out that the value of θ_s depends on whether the harmonic confinement is present or not.

In Fig. 11 we plot the magnetization on the right side for square (top panel) and hexagonal (bottom panel) moiré patterns for $N = 300$. In each panel we include two different values of the twisting angle θ. Curves in yellow tones are associated with $\theta = 30°$ and $25°$ for square and hexagonal lattices, respectively, and curves in purple tones correspond to $\theta = 5°$ for both geometries. To illustrate the dependence
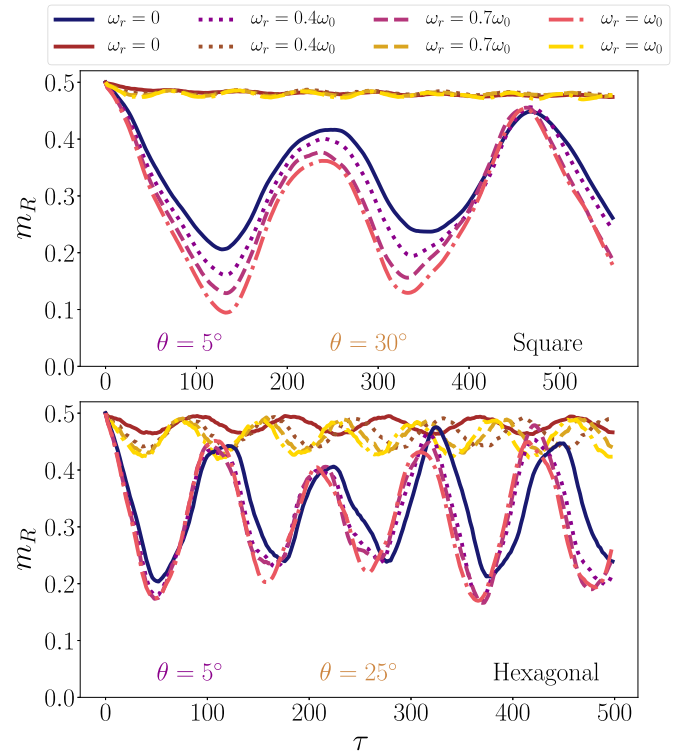

FIG. 11. Magnetization as a function of time in the right side for moiré patterns created from the superposition of primitives square (top panel) and hexagonal (bottom panel) rotated an angle θ. Curves in yellow tones correspond to $\theta = 30°$ and $25°$ for square and hexagonal lattices, and curves in purple tones are associated with $\theta = 5°$ for both kinds of geometries. The effective interaction coupling $g_{\downarrow\downarrow} = 4\pi N\hbar^2 a_2/m$ and $g_{\downarrow\uparrow} = 4\pi N\hbar^2/m(\frac{2a_0+a_2}{3})$ with $N = 300$.

of $m_R(\tau)$ on the moiré structures under the presence of a harmonic confinement, we chose four different values of the frequencies $\omega_r = \omega_r = 0, 0.4\omega_0, 0.7\omega_0$, and ω_0. The behavior as a function of time for different values of these frequencies was identified with solid, dotted, dashed, and dashed-dotted lines, respectively. Similarly to the noninteracting case, m_R shows an oscillatory behavior for $\theta = 5°$ (see purple curves in both panels of Fig. 11), with the role of the harmonic confinement captured as a limited shift with respect to $\omega_r/\omega_0 = 0$. The net effect of the effective mean-field interaction $g_{\sigma\sigma'} \neq 0$ against the noninteracting scenario is the diminishing of the oscillation period of m_R. Interestingly, yellow curves associated with $\theta = 30°$ and $25°$ for square and hexagonal lattices, respectively, exhibit an oscillatory behavior reminiscent of that observed in Figs. 4 and 5, but with a small amplitude.

To illustrate the influence that the moiré structures have on preserving the initial state, we followed the dynamics of $m_R(\tau)$ in the whole interval of rotation angles that give rise to the formation of square and hexagonal moiré patterns for three different values of N. In the panels of Fig. 12 we plot in a density color scheme the behavior of $m_R(\tau)$ for $\omega_r = \omega_0$ for square (top panels) and hexagonal (bottom panels) moiré structures for different values of N, from left to right $N = 300, 600$, and 900. As can be appreciated from these panels, the marked variations of $m_R(\tau)$ for $\theta \in [0°, 45°]$ and $[0°, 30°]$ for square and hexagonal lattices, respectively, are
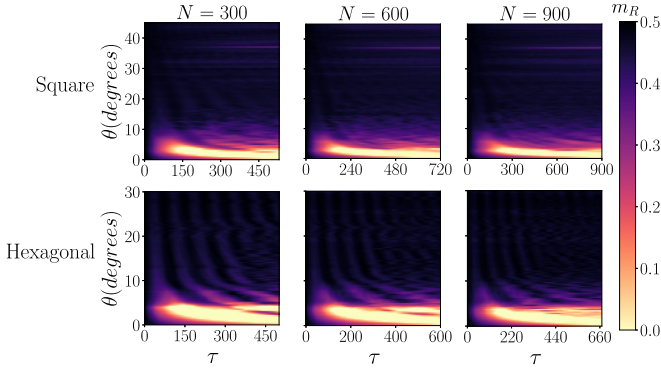
FIG. 12. Magnetization as a function of time in the right side in the density color scheme for moiré patterns created from the superposition of primitives square (top panels) and hexagonal (bottom panels) rotated an angle θ, for $\omega_0 = \omega_r$. Each panel corresponds to a given value of the N in the effective interaction coupling $g_{\downarrow\downarrow} = 4\pi N \hbar^2 a_2/m$ and $g_{\downarrow\uparrow} = 4\pi N \hbar^2/m(\frac{2a_0 + a_2}{3})$ with $N = 300$.

mostly restricted to certain angles. We observe from these figures that moiré patterns arising from rotation angles larger than $\theta \gtrsim 10°$ constitute structures in which the initial state is preserved, with the exception of Pythagorean angles in the case of the square symmetry. It is worth noticing, as in the noninteracting case, that decreasing of magnetization is observed for angles that satisfy Diophantine equations. To illustrate this behavior in Fig. 13 we plot the magnetization in square (top panel) and hexagonal (bottom panel) patterns for two different angles. Solid and dashed lines correspond to rotation angles associated with a given moiré structure. Dashed lines label angles that satisfy a particular Diophantine equation. (m, n, l) triples are $(4,3,5)$ and $(3,5,7)$ for square and hexagonal symmetries, respectively. While in the case of the square moiré lattice one observes a decay of m_R, a slowdown in the dynamics is appreciated for the hexagonal lattice.

A general conclusion that can be outlined from the time evolution of the initial double ferromagnetic state is that a dynamic stability emerges for certain rotation angles in both square and hexagonal moiré patterns. In other words, we found that the qualitative behavior of m_R is dominated by the moiré structure against the influence of both the mean-field interactions and the presence of the harmonic confinement. Certainly, by looking at the detailed quantitative behavior of m_R one can appreciate differences between the noninteracting and interacting cases (see Figs. 4, 5, and 11). Also, it is important to stress that the dynamics, that is, oscillations between $\uparrow$ and $\downarrow$ in left and right sides, takes place at the central region where the spin components share a frontier.

IV. CONCLUSIONS

We have investigated the time dynamics of a two-component weakly interacting Bose gas lying in moiré patterns with square or honeycomb symmetries. The patterns considered are the result of superimposing two primitive square or hexagonal lattices lying on top of each other, rotated by an angle θ, plus the presence of an isotropic harmonic confinement in 2D. The system, far away from the Mott insulating
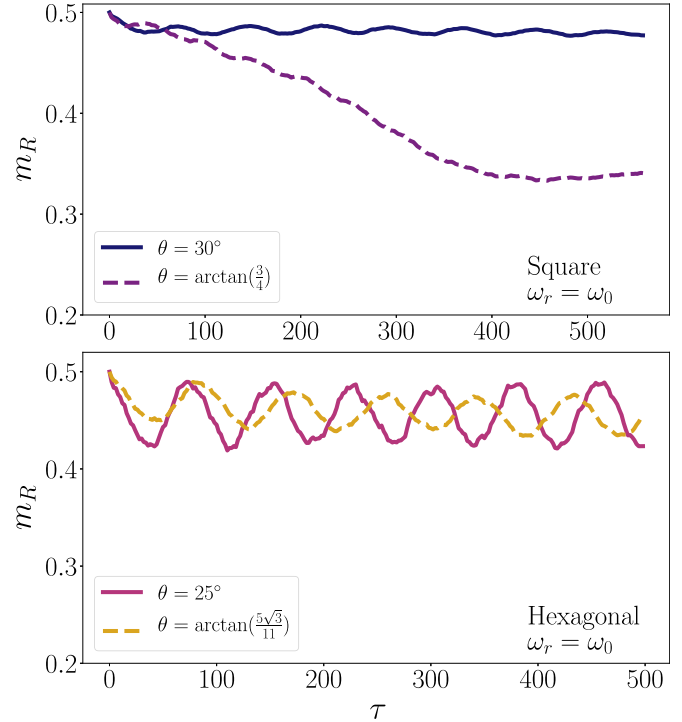

FIG. 13. Magnetization as a function of time in the right side for square (top panel) and hexagonal (bottom panel) moiré lattices. Solid and dashed lines indicate the rotation angles associated with a given moiré structure. Dashed lines correspond to angles that satisfy a particular Diophantine equation for square and hexagonal symmetries. $\omega_0 = \omega_r$ and the effective interaction coupling $g_{\downarrow\downarrow} = 4\pi N \hbar^2 a_2/m$ and $g_{\downarrow\uparrow} = 4\pi N \hbar^2/m(\frac{2a_0 + a_2}{3})$ with $N = 300$.

regime, was described within the mean-field approach through the time dependent Gross-Pitaevskii equation that was solved for lattices with a number of sites up to $\approx 90 \times 90$.

The initial state was prepared by situating two different hyperfine spin components of an $F = 1$ ^{23}Na Bose-Einstein condensate on the left and right sides of a given moiré lattice, and then allowed to evolve under the influence of the effective mean-field interactions, the potential created from the superposition of the rotated lattices, and the isotropic harmonic confinement. In our paper we considered both cases, the noninteracting and the weakly interacting ones. ^{23}Na were the atoms considered in the investigation since the nature of their ground-state $F = 1$ spinor components is polar and thus the hyperfine components can mix during its time evolution. We identified particular values of the rotation angle θ for which a dynamic stability is found. The angles belong to the interval $[\theta_s, 45°]$ and $[\theta_s, 30°]$ for square and hexagonal lattices, respectively, θ_s being an angle that depends on whether interactions are considered or not. In the interacting case $\theta_s \approx 10°$, this value being independent of the harmonic frequency. In contrast, in the noninteracting case, θ_s depends both on the presence of the harmonic confinement and the lattice geometry. We must stress that in the case of square lattices the dynamic stability is damaged for angles $\theta = \arctan n/m$, n and m being part of the triple (m, n, l) that satisfies $m^2 + n^2 = l^2$. In case of the hexagonal lattice, the dynamic stability is unaffected for angles satisfying $\tan \theta = n\sqrt{3}/(2m + n)$ with

$m^2 + n^2 + nm = l^2$, where $m, n, l \in \mathbb{Z}$ in both lattices. Also it is important to accentuate that the role of the interaction is to reduce the magnetization oscillation amplitude. These results are reminiscent of the phenomenon in which light localizes in photonic moiré lattices [41].

In summary, we conclude that although the confinement provided by the harmonic trap and the effective mean-field interactions play an important role on the dynamics of the double magnetic domain, the dominant effect behind the occurrence of the dynamic stability is provided by moiré lattices. The role of the twisting angle is crucial to identify the sharp transition towards the dynamic stability.

The investigation here presented adds to the understanding of properties that arise in moiré lattices in 2D. While the proposal here presented employs the ultracold quantum gases as an ideal platform to set and probe the dynamics of particles moving in a moiré structure, graphene moiré heterostructures have been suggested as a condensed-matter quantum simulator [42] to explore elusive states of matter in the laboratory. In both cases the prominent conclusion is the existence and identification of the special or magic twisting angles for which an abrupt transition happens. In this sense our analysis is relevant within the current context of the design of quantum materials belonging to the emerging field of twistronics.

APPENDIX A: SQUARE AND HEXAGONAL MOIRÉ CRYSTALS

In this Appendix we briefly revisit the discussion of the stationary moiré patterns used to prepare the initial states. The large size of the lattices considered in our paper, namely, 90×90 sites, allowed us to establish several conclusions regarding the twisting angle and the patterns emerging from the superposition of the lattices. From the stationary density profiles of each component, for a frequency $\omega_r = 0$, we observe that starting at low angles of relative rotation the so-called moiré crystals appear [15,43]. These moiré crystals, also called superlattices, are characterized by having a lattice constant that depends on the twisting angle θ. We observe that such lattices are present for twisting angles in the intervals $\theta \in (0°, 30°)$ and $(0°, 45°)$ for hexagonal and square geometries, respec-
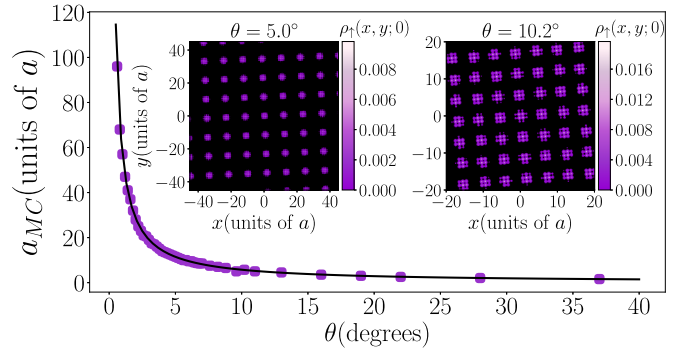

FIG. 14. Lattice constant a_{MC} of square moiré crystals as a function of the twisting angle θ. Dots in this curve are fitted by the formula in Eq. (A1) (solid line). The insets show the superfluid density of the stationary state for one of the spin components for two different rotation angles. The purple color scheme in the bar indicates the size of the superfluid density. Left and right sides correspond to $\theta = 5°$ and $10.2°$, respectively.

tively. In Figs. 14 and 15 we plot the lattice constant a_{MC} as a function of the angle θ. The lattice constant of the superlattice is measured in units of the lattice parameter a that characterizes the original square and hexagonal structures. To illustrate the dependence of the lattice constant a_{MC} on the twisting angle θ, in Figs. 14 and 15, besides the behavior of a_{MC} vs θ, we show in the insets a couple of density profiles for the single component $\Psi_\uparrow$ associated with two different values of θ. The amplitude of the profiles is shown in a density color scheme scaled with the bar at the right of the insets. As one can see from these profiles, instead of observing sharply defined spots of the superfluid density, we observe a basis of patterns at each *node* of the superlattice. We notice how these patterns inherit the symmetry of the original square and hexagonal structures. It is important to point out that in the case of moiré lattices arising from hexagonal patterns two superlattices emerge as a result of the relative rotation between the original lattices. These lattices having hexagonal and triangular symmetries are such that, for some values of the twisting angle, one of them has a density profile with a larger intensity with respect to the other (see in Fig. 15 the color density scheme at the bar on the right of each profile). Purple and green colors correspond to triangular and hexagonal moiré crystals.

TABLE I. Parameters for the numerical simulation.

Name	Symbol	Value
Number of grid points in the x direction	N_x	512–1024
Number of grid points in the y direction	N_y	512–1024
Spatial extension of the numerical grid in the x direction	L_x	40–90 a
Spatial extension of the numerical grid in the y direction	L_y	40–90 a
Step size used in real time evolution	$d\tau$	0.0005

TABLE II. Physical parameters used in the numerical simulation.

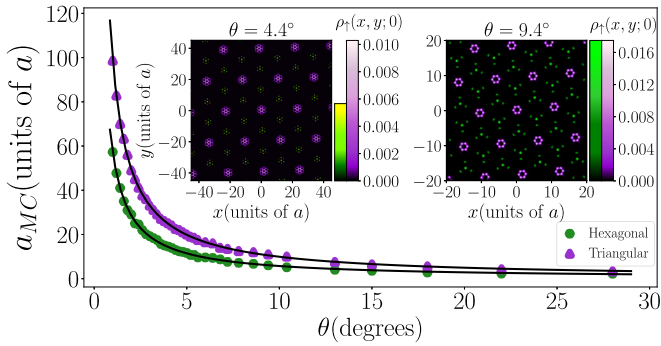| Name	Symbol	Value
Particle number	N	300, 600, 900
^{23}Na mass	m	22.989 amu
Lattice constant	a	532 nm
Reference trap frequency	ω_0	$2\pi \times 50$ rad/s
Trap frequency (z)	ω_z	$2\pi \times 5000$ rad/s
Bare s-wave scattering length for the 0 canal	a_0	50.0 a_B
Bare s-wave scattering length for the 2 canal	a_2	55.1 a_B
Potential depth	V_0	2 E_R

FIG. 15. Lattice constant a_{MC} of hexagonal moiré crystals as a function of the twisting angle θ. Purple and green dots in the curves are fitted by the formula in Eq. (A1) (solid lines) and correspond to two superimposed triangular and hexagonal lattices, that emerge when two hexagonal lattices are rotated an angle θ. The insets show the superfluid density of the stationary state for one of the spin components for two different rotation angles. Purple and green density color schemes in the bars indicate the size of the superfluid density. Left and right sides correspond to $\theta = 4.4°$ and $9.4°$, respectively.

The formula that fits the dependence of a_{MC} as a function of θ for the superlattice is [15,43]

$$a_{MC} = \frac{a}{nc_1 \sin(\theta/c_2 n)}, \qquad (A1)$$

where n is a nonzero integer number, and $c_1 = c_2 = 1$ for the square and hexagonal moiré crystals, while $c_1 = 1.56$ and $c_2 = 2.70$ for the triangular moiré crystal.

As expected, the moiré patterns that result from two superimposed square and hexagonal structures, for the particular angles $\theta = 45°$ and $30°$, have octagonal and hexagonal quasicrystalline geometries, respectively. In Fig. 16 we illustrate these quasicrystalline structures associated to $\uparrow$ and $\downarrow$
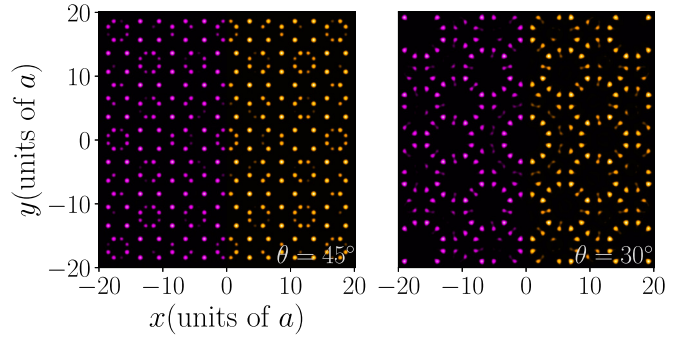

FIG. 16. Density profiles prepared from the superposition of two rotated square (left) and two rotated hexagonal (right) lattices, the rotation angles being $\theta = 45°$ and $30°$, respectively. For those angles the resulting structures are quasicrystals with octagonal and hexagonal rotation symmetry. Left (purple) and right (yellow) sides in each panel correspond to the superfluid density associated with the pseudospin components $\downarrow$ and $\uparrow$, respectively. Frequency of the harmonic trap is $\omega_r = 0$.

components for the case in which the harmonic confinement is absent. Those quasicrystalline moiré patterns shall also be considered as the initial state, to follow its time evolution.

APPENDIX B: NUMERICAL CALCULATION DETAILS

The results here reported were obtained from numerical solution of the coupled GP equations. In this Appendix we present additional details related to the technical part of the calculations performed. To find the solution of Eq. (1) we use the fourth-order Runge-Kutta method, which we used both to obtain the ground state and to study the dynamics of the system. The numerical parameters used for the simulations are shown in Table I, while the physical parameters of the system are presented in Table II.

[1] Y. Wang, Z. Wang, W. Yao, G.-B. Liu, and H. Yu, Phys. Rev. B **95**, 115429 (2017).

[2] L. A. Ponomarenko, R. V. Gorbachev, G. L. Yu, D. C. Elias, R. Jalil, A. A. Patel, A. Mishchenko, A. S. Mayorov, C. R. Woods, J. R. Wallbank, M. Mucha-Kruczynski, B. A. Piot, M. Potemski, I. V. Grigorieva, K. S. Novoselov, F. Guinea, V. I. Fal'ko, and A. K. Geim, Nature (London) **497**, 594 (2013).

[3] C. R. Dean, L. Wang, P. Maher, C. Forsythe, F. Ghahari, Y. Gao, J. Katoch, M. Ishigami, P. Moon, M. Koshino, T. Taniguchi, K. Watanabe, K. L. Shepard, J. Hone, and P. Kim, Nature (London) **497**, 598 (2013).

[4] B. Hunt, J. D. Sanchez-Yamagishi, A. F. Young, M. Yankowitz, B. J. LeRoy, K. Watanabe, T. Taniguchi, P. Moon, M. Koshino, P. Jarillo-Herrero, and R. C. Ashoori, Science **340**, 1427 (2013).

[5] Y. Cao, V. Fatemi, S. Fang, K. Watanabe, T. Taniguchi, E. Kaxiras, and P. Jarillo-Herrero, Nature (London) **556**, 43 (2018).

[6] Y. Cao, V. Fatemi, A. Demir, S. Fang, S. L. Tomarken, J. Y. Luo, J. D. Sanchez-Yamagishi, K. Watanabe, T. Taniguchi, E. Kaxiras, R. C. Ashoori, and P. Jarillo-Herrero, Nature (London) **556**, 80 (2018).

[7] F. Xiao, K. Chen, and Q. Tong, Phys. Rev. Res. **3**, 013027 (2021).

[8] X.-J. Zhao, Y. Yang, D.-B. Zhang, and S.-H. Wei, Phys. Rev. Lett. **124**, 086401 (2020).

[9] G. Tarnopolsky, A. J. Kruchkov, and A. Vishwanath, Phys. Rev. Lett. **122**, 106405 (2019).

[10] F. Yndurain, Phys. Rev. B **99**, 045423 (2019).

[11] A. Lopez-Bezanilla, Phys. Rev. Mater. **3**, 054003 (2019).

[12] K. Seo, V. N. Kotov, and B. Uchoa, Phys. Rev. Lett. **122**, 246402 (2019).

[13] H. Pan, F. Wu, and S. Das Sarma, Phys. Rev. B **102**, 201104(R) (2020).

[14] A. González-Tudela and J. I. Cirac, Phys. Rev. A **100**, 053604 (2019).

[15] Z. Meng, L. Wang, W. Han, F. Liu, K. Wen, C. Gao, C. Chinand, and J. Zhang, Nature **615**, 231 (2023).

[16] R. Mahmood, A. Vela Ramirez, and A. C. Hillier, ACS Appl. Nano Mater. **4**, 8851 (2021).

[17] J.-Y. Choi, S. Hild, J. Zeiher, P. Schauβ, A. Rubio-Abadal, T. Yefsah, V. Khemani, D. A. Huse, I. Bloch, and C. Gross, Science **352**, 1547 (2016).

[18] F. Schäfer, T. Fukuhara, S. Sugawa, Y. Takasu and Y. Takahashi, Nat. Rev. Phys. **2**, 411 (2020).

[19] N. N. Klausen, J. L. Bohn and C. H. Greene, Phys. Rev. A **64**, 053602 (2001).

[20] Z. Z. Hadzibabic, P. Krüger, M. Cheneau, B. Battelier, and J. Dalibard, Nature (London) **441**, 1118 (2006).

[21] C-L. Hung, X. Zhang, N. Gemelke, and C. Chin, Nature (London) **470**, 236 (2011).

[22] T.-L. Ho, Phys. Rev. Lett. **81**, 742 (1998).

[23] A. Crubellier, O. Dulieu, F. Masnou-Seeuws, M. Elbs, H. Knöckel, and E. Tiemann, Eur. Phys. J. D. **6**, 211 (1999).

[24] A. Posazhennikova, Rev. Mod. Phys. **78**, 1111 (2006).

[25] L. Salasnich, A. Parola, and L. Reatto, Phys. Rev. A **65**, 043614 (2002).

[26] A. Muñoz Mateo and V. Delgado, Phys. Rev. A **77**, 013617 (2008).

[27] W. Bao, D. Jaksch, and P. A. Markowich, J. Comput. Phys. **187**, 318 (2003).

[28] C. Trallero-Giner, R. Cipolatti, and T. C. H. Liew, Eur. Phys. J. D **67**, 143 (2013).

[29] R. Zamora-Zamora, G. A. Domínguez-Castro, C. Trallero-Giner, R. Paredes, and V. Romero-Rochín, J. Phys. Commun. **3**, 085003 (2019).

[30] D. S. Petrov, M. Holzmann, and G. V. Shlyapnikov, Phys. Rev. Lett. **84**, 2551 (2000).

[31] S. Ray, M. Pandey, A. Ghosh, and S. Sinha, New J. Phys. **18**, 013013 (2016).

[32] T. Schulte, S. Drenkelforth, J. Kruse, R. Tiemeyer, K. Sacha, J. Zakrzewski, M. Lewenstein, W. Ertmer, and J. J. Arlt, New J. Phys. **8**, 230 (2006).

[33] S. K. Adhikari and L. Salasnich, Phys. Rev. A **80**, 023606 (2009).

[34] A. Michelangeli and A. Olgiati, J. Nonlinear Math. Phys. **24**, 426 (2017).

[35] C. Madroñero, G. A. Domínguez-Castro, L. A. González-García, and R. Paredes, Phys. Rev. A **102**, 033304 (2020).

[36] The grid used in our numerical calculations was 512×512. All the calculations were implemented in state of the art GPU hardware.

[37] R. Dum and Y. Castin, Eur. Phys. J. D **7**, 399 (1999).

[38] R. Zeng and Y. Zhang, Comput. Phys. Commun. **180**, 854 (2009).

[39] D. M. Weld, P. Medley, H. Miyake, D. Hucul, D. E. Pritchard, and W. Ketterle, Phys. Rev. Lett. **103**, 245301 (2009).

[40] S. Palacios Alvarez, P. Gomez, S. Coop. R. Zamora-Zamora, C. Mazzinghi and M. Mitchel, Proc. Natl. Acad. Sci. USA **119**, e2115339119 (2022).

[41] P. Wang, Y. Zheng, X. Chen, Ch. Huang, Y. V. Kartashov, L. Torner, V. V. Konotop, and F. Ye, Nature (London) **577**, 42 (2020).

[42] D. M. Kennes, M. Claassen, L. Xian, A. Georges, A. J. Millis, J. Hone, C. R. Dean, D. N. Basov, A. N. Pasupathy, and A. Rubio, Nat. Phys. **17**, 155 (2021).

[43] M. Feuerbacher, Acta Cryst. **A77**, 460 (2021).